COBEM 99
XV Congresso Brasileiro de Engenharia Mecânica
15th Brazilian Congress of Mechanical Engineering
22 - 26 de Novembro de 1999 / November 22 - 26, 1999 Águas de Lindóia, São Paulo,

3-D MODELING OF MODE I CRACK GROWTH IN STRUCTURAL MATERIALS

Claudio Ruggieri
Department of Naval Architecture and Ocean Engineering, University of São Paulo
São Paulo, SP 05508–900, E-mail: cruggi@usp.br, Brazil

Robert H. Dodds, Jr.
Department of Civil Engineering, University of Illinois at Urbana-Champaign
Urbana, IL 61801, E-mail: r-dodds@uiuc.edu, US

Abstract *– This study describes a 3-D computational framework to model stable extension of a macroscopic crack under mode I conditions in ductile metals. The Gurson-Tvergaard dilatant plasticity model for voided materials describes the degradation of material stress capacity. Fixed-size, computational cell elements defined over a thin layer at the crack plane provide an explicit length scale for the continuum damage process. Outside of this layer, the material remains undamaged by void growth, consistent with metallurgical observations. An element vanish procedure removes highly voided cells from further consideration in the analysis, thereby creating new traction-free surfaces which extend the macroscopic crack. The key micro-mechanics parameters are D, the thickness of the computational cell layer, and f_0, the initial cell porosity. Calibration of these parameters proceeds through analyses of ductile tearing to match R-curves obtained from testing of deep notch, through-crack bend specimens. The resulting computational model, coupled with refined 3-D meshes, enables the detailed study of non-uniform growth along the crack front and predictions of specimen size, geometry and loading mode effects on tearing resistance, here described by J-Δa curves. Computational and experimental studies are described for shallow and deep notch SE(B) specimens having side-grooves and for a conventional C(T) specimen without side-grooves. The computational models prove capable of predicting the measured R-curves and post-test measured crack profiles.*

Key words*: ductile fracture, computational cells, Gurson model, finite elements, constraint*

1. INTRODUCTION

The stable tearing of a macroscopic crack in ductile materials for structural applications, such as steel alloys and aluminum, is conventionally characterized by crack growth resistance (J–Δa) curves using the J-integral to describe the intensity of near-tip deformation (see, e.g., the review by Hutchinson [1]). Since additional load-carrying capacity in structural components is gained if some amount of stable crack growth is allowed, a large number of engineering applications, particularly predictions of mechanical behavior and defect assesments of in-service structure, currently centers on methodologies based upon measured R-curves. Specifically, large increases of J above the onset of ductile crack extension (J_{Ic}) are possible in materials with high tearing resistance with considerable practical consequences to design and structural flaw analysis. Moreover, ductile tearing often preceeds cleavage fracture in structural steels

operating in the ductile-to-brittle (DBT) region; such small amounts of stable crack growth alter significantly the near-tip stress fields [2,3] which strongly affect the propensity to trigger cleavage.

Laboratory testing of fracture specimens to measure resistance curves (J-Δa) consistently reveals a marked effect of absolute specimen size, geometry, relative crack size (a/W) and loading mode (tension *vs.* bending) on R-curves (see [4] for representative experimental studies). For the same material, deep-notch bend, SE(B), and compact tension, C(T), specimens yield low R-curves while shallow-notch SE(B)s, single-edge notch tension, SE(T), and middle-crack tension, M(T), specimens yield larger toughness values at similar amounts of crack growth. These effects observed in R-curves arise from the strong interaction between microstructural features of the material which govern the actual separation process and the loss of stress triaxiality in the crack front region due to large-scale yielding. Consequently, realistic methodologies for fracture assessments of structural components must include advanced procedures capable of modeling ductile crack extension.

This study extends the *computational cell* framework, originally developed in a 2-D context by Xia and Shih (X&S) [5,6,7] into a 3-D setting capable of modeling mode I crack extension. Applications of this 3-D framework readily include, for example, surface breaking defects as well as conventional, through-thickness fracture specimens (with and without side-grooves). In the computational cell model, ductile crack extension occurs through void growth and coalescence (by cell extinction) within a thin layer of material symmetrically located about the crack plane. An element vanish procedure removes highly voided cells from the analysis thereby creating new traction-free surfaces which extend the macroscopic crack. The cells have initial (smeared) void volume fraction denoted by f_0. The layer thickness (D) introduces a strong length-scale over which damage occurs; elsewhere, the background material obeys the flow theory of plasticity without damage by void growth. The 3-D form of the Gurson-Tvergaard (GT) dilatant plasticity theory [8,9] provides a suitable description of void growth within the cells. Our exploratory 3-D studies using computational cells clearly demonstrate the capability to predict the strong constraint effects on measured R-curves and severe tunneling in non-side-grooved specimens. The resulting computational framework, coupled with refined 3-D meshes, enables the detailed study of non-uniform growth along the crack front and development of improved models to assess fracture behavior in structural materials.

2. COMPUTATIONAL CELL MODEL FOR DUCTILE CRACK GROWTH

Ductile fracture in metals is a multistep mode of material failure incorporating the combination of various and simultaneous mechanisms at the microscale level (see, e.g., the review of Garrinson and Moody [10]). Such mechanisms are conveniently divided as follows: a) nucleation of microvoids from fracture or separation of inclusions, b) subsequent growth of widely separated and larger microvoids, c) localization of plastic flow and d) final coalescence of microvoids. Unlike cleavage fracture, which is a mechanism driven almost entirely by the local tensile stresses, inclusion of the microregime of ductile fracture in crack growth analyses is central to relate the material tearing behavior with a macroscopic (engineering) fracture parameter in a continuum framework. Experimental observations and computational studies show that the plastic strains for nucleation are small thereby causing only little damage in the material ahead of the crack tip. Such feature enables simplification of the four-step failure process described above by assuming the growth of microvoids as the critical event controling ductile extension. Figure 1(a) pictures the schematic path of a growing crack in a ductile material. The material layer enveloping the growing crack, which must be thick enough to include at least a void or microcrack nuclei, identifies a process zone for the ductile fracture which conveniently gives the necessary length dimension for the model. Void growth and coalescence in the layer will cause the surface tractions that the process zone exerts on its surrounding drop to zero (this implicitly defines a traction-separation law for the process zone layer).

Motivated by the above observations, X&S [5,6,7] proposed a model using *computational cells* to include a realistic void growth mechanism, and a microstructural length-scale physical-

ly coupled to the size of the fracture process zone. Void growth remains confined to a layer of material symmetrically located about the crack plane, as illustrated in Fig. 1(b), and having thickness D, where D is associated with the mean spacing of the larger, void initiating inclusions. This layer consists of cubical cell elements with dimension D on each side; each cell contains a cavity of initial volume fraction f_0 (the initial void volume divided by cell volume). As a further simplification, the void nucleates from an inclusion of relative size f_0 immediately upon loading. Progressive void growth and subsequent macroscopic material softening in each cell are described with the Gurson-Tvergaard (GT) constitutive model for dilatant plasticity [8,9] given by

$$g(\sigma_e, \sigma_m, \bar{\sigma}, f) = \left(\frac{\sigma_e}{\bar{\sigma}}\right)^2 + 2q_1 f \cosh\left(\frac{3q_2\sigma_m}{2\bar{\sigma}}\right) - \left(1 + q_3 f^2\right) = 0 \tag{1}$$

where σ_e denotes the effective Mises (macroscopic) stress, σ_m is the mean (macroscopic) stress, $\bar{\sigma}$ is the current flow stress of the cell matrix material and f defines the current void fraction. Under multiaxial stress states, $\sigma_e = (3S_{ij}S_{ij}/2)^{1/2}$ where S_{ij} denotes the deviatoric components of Cauchy stress. Factors q_1, q_2 and q_3 introduced by Tvergaard improve the model predictions for periodic arrays of cylindrical and spherical voids. Following Tvergaard we use $q_1 = 1.25$, $q_2 = 1.0$ and $q_3 = q_1^2$.

An additional contribution to the void growth rate arises from the nucleation of new voids caused by large plastic strains at much stronger, smaller inclusions dispersed into the matrix. The volume fraction of voids increases over an increment of load due to continued growth of existing voids and due to the formation of new voids caused by interfacial decohesion of inclusions or second phase particles. Thus,

$$df = (1 - f)d\epsilon^p_{kk} + \mathcal{A}(\bar{\epsilon}^p)d\bar{\epsilon}^p = (1 - f)d\epsilon^p_{kk} + \frac{f_N}{s_N\sqrt{2\pi}}\exp\left[-\frac{1}{2}\left(\frac{\bar{\epsilon}^p - \epsilon_N}{s_N}\right)^2\right]d\bar{\epsilon}^p \tag{2}$$

where $\bar{\epsilon}_p$ denotes the matrix plastic strain and ϵ^p is the volumetric (macroscopic) plastic strain. Here, the nucleation component follows a normally distributed evolution model [12] with parameter $\mathcal{A}$ defined by the mean value, ϵ_N, the standard deviation, s_N and the volume fraction of void nucleating particles, f_N.

The GT yield function in Eq. (1) does not model realistically the rapid loss of stress capacity for larger void fractions nearing coalescence levels, nor does the model create new traction free surfaces to represent physical crack extension. In the present work, the evolution of stress within cells follows the original constitutive model of GT in Eq. (1) until $f = f_E$, where f_E typically has a value of ≈ 0.15. The final stage of void linkup with the macroscopic crack front then occurs by reducing the remaining stresses to zero in a prescribed manner. Tvergaard [9] refers to this process as the element extinction or vanish technique. Our cell extinction process implements a linear-traction separation model (see additional details in Ruggieri and Dodds (R&D) [11]). When f in the cell incident on the current crack tip reaches a critical value, f_E, the computational procedures remove the cell thereby advancing the crack tip in discrete increments of the cell size.

Figure 1(c) shows the typical, plane strain finite element representation of the computational cell model where symmetry about the crack plane requires elements of size $D/2$. Material outside the computational cells, the "background" material, follows a conventional J_2 flow theory of plasticity and remains undamaged by void growth in the cells. Material properties required for this methodology include: for the background material Young's modulus (E), Poisson's ratio (ν), yield stress (σ_0) and hardening exponent (n) or the actual measured stress-strain curve; and for the computational cells: D and f_0 (and of much less significance f_E). The background material and the matrix material of the cells generally have identical flow properties. Using an experimental J-Δa curve obtained from a conventional SE(B) or C(T) specimen, a series of finite element analyses of the specimen are conducted to calibrate values for the cell parameters D and f_0 which bring the predicted J-Δa curve into agreement with experiment. The

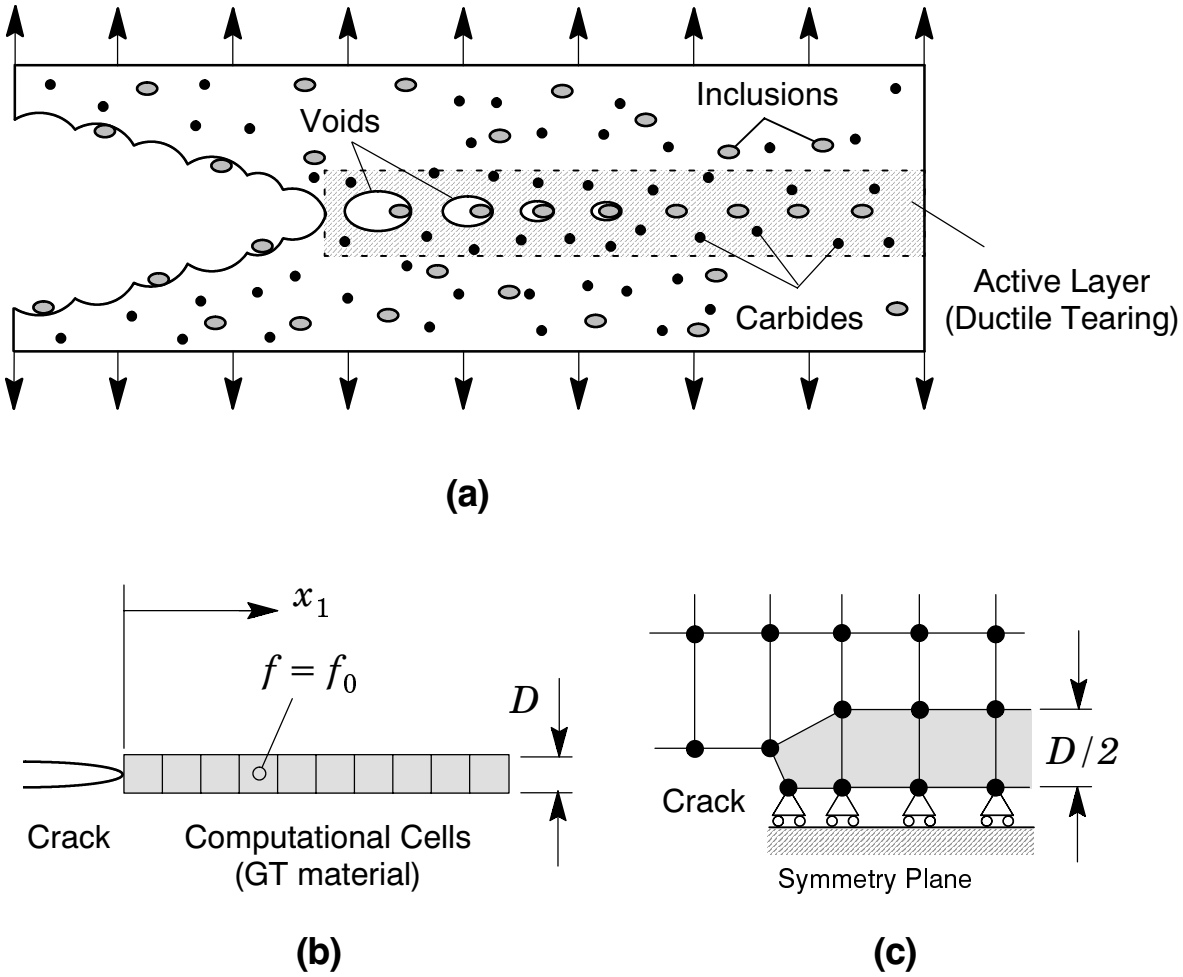

Figure 1 Modeling of ductile tearing using computational cells.

CTOD at initiation of ductile tearing provides a good starting value for D, with f_0 then varied to obtain agreement with the experiment. Alternatively, metallurgical surveys of inclusion volume fractions and sizes may be used with various packing arrangements (e.g. nearest neighbor distance) to estimate D and/or f_0 . Experience with plane-strain finite element analyses of SE(B) and C(T) specimens to estimate D and f_0 for common structural and pressure vessel steels suggests values of 50-200 μm for D, 0.001-0.005 for f_0 , with f_E typically 0.15-0.20. Once determined in this manner using a specific experimental R-curve, D and f_0 become "material" parameters and remain fixed in analyses of all other specimen geometries for the same material.

The three-dimensional computations for the crack growth analyses reported here are generated using the research code WARP3D [13]. Key features of the code employed in this work include: (1) the GT and Mises constitutive models implemented in a finite-strain setting, (2) cell extinction using the traction-separation model, (3) automatic load step sizing based on the rate of damage accumulation, and (4) evaluation of the J-integral using a domain integral procedure. WARP3D employs a continuously updated, Lagrangian formulation naturally suited for solid elements having only translational displacements at the nodes. For these large, 3-D analyses which typically require 1500 or more solutions of the linearized equations, an exceptionally fast code/solver becomes critical to render the analyses computationally feasible. WARP3D solves the equations at each iteration using a linear pre-conditioned conjugate gradient (LPCG) method implemented within an element-by-element (EBE) software architecture.

This approach reduces memory sizes and execution times significantly below those for sparse direct solvers (no assembly of the system stiffness matrix).

3. FINITE ELEMENT MODELS

3.1. SE(B) Specimens

Finite element analyses are described for shallow notch ($a/W = 0.14$) and deep notch ($a/W = 0.6$) 1T-SE(B) specimens with thickness, B, of 25.4 mm. Here a denotes the crack length and W the specimen width. Joyce and Link [15] performed unloading compliance tests at 100°C on these specimens made of ASTM A533B (TL orientation) to measure tearing resistance curves in terms of J-Δa. After fatigue pre-cracking, the specimens were side-grooved to a depth of $0.1B$ on each side to promote uniform ductile growth over the thickness. The analyses utilize a piecewise-linear approximation for the measured true stress-logarithmic strain curve constructed from the average of three tensile tests (see additional details in R&D [11]). Other mechanical properties needed for the analyses include $E = 200$ GPa and $\nu = 0.3$. The matrix material of the computational cell elements and the void-free background material are assigned these properties.

Figure 2(a) shows the finite element model constructed for 3-D analyses of the specimen with $a/W = 0.6$. The shallow crack model has similar features. Symmetry conditions enable analyses using one-quarter, 3-D models and one-half, plane-strain models. The 3-D models have approximately 8000 isoparametric 8-node elements arranged into 13, variable thickness layers over the half-thickness ($B/2$), as illustrated in Fig. 2 (a). The first 9 layers lie along the crack front and the outermost 4 layers define the side groove region; each layer has the identical "in-plane" (X-Y) mesh refinement. Within each of the 9 layers over the crack front, the element mesh contains a row of 60 computational cells along the remaining ligament ($W - a$) arranged as shown in Fig. 1(c). A series of calibration analyses suggest an optimal cell size of $D = 250\,\mu$m. The initially blunted crack tip accommodates the intense plastic deformation and initiation of stable crack growth in the early part of ductile tearing. The *slab* of 540 (9×60) computational cells over which damage occurs to model crack growth extends 7.5 mm ahead of the initial crack front.

Appropriate constraints are imposed on the symmetry planes for all configurations. Displacement controlled loading of the models as indicated in Fig. 2(a) permits continuation of the analyses once the load decreases during crack growth. For both a/W ratios, multiple sets of nodes on $Y = 0$ near the top surface must have imposed displacements to prevent locally severe, element distortions. A typical solution to advance the crack by 40 cells ($\Delta a = 40 \times D/2 = 5$ mm) on the centerplane ($Z = 0$) in the deep crack specimen uses 700 load increments and requires 3 CPU hours on a CRAY C-90 supercomputer.

3.2. C(T) Specimens

Finite element analyses in a full 3-D setting are conducted on a deep crack ($a/W = 0.68$), 1T-C(T) specimen with thickness, B, of 25.4 mm that has no side grooves. Here a denotes the crack length and W the specimen width. Panontin and Nishioka [16] performed unloading compliance tests at room temperature on specimens made of ASTM A516 to measure tearing resistance curves in terms of J-Δa. The experimental matrix includes specimens in both T-L and L-T orientations. The analyses utilize a piecewise-linear approximation for the measured true stress-logarithmic strain curve constructed from the average of three tensile tests (see additional details in R&D [11]). Other mechanical properties needed for the analyses include $E = 200$ GPa and $\nu = 0.3$.

Figure 2(b) shows the finite element model constructed for 3-D analyses of the C(T) specimen. The quarter-symmetric, 3-D model has 5432 isoparametric 8-node elements arranged

into 7 variable thickness layers defined over the half thickness with appropriate constraints imposed on the symmetry plane. This refinement in the thickness direction proved satisfactory to resolve the tunneled crack front profile. Displacement controlled loading applied at the pin hole indicated in Fig. 2(b) enables continuation of the analyses once the load decreases during crack growth. Within each of the 7 layers over the crack front, the element mesh contains a row of 60 computational cells along the remaining ligament $(W-a)$ arranged as shown in Fig. 2(b). A series of calibration analyses suggest an optimal cell size of $D = 200\,\mu$m for this material. The initially blunted crack tip accommodates the intense plastic deformation and initiation of stable crack growth in the early part of ductile tearing. The *slab* of 420 (7×60) computational cells over which damage occurs is capable of accommodating ≈ 4 mm of growth on the center-plane ahead of the initial crack front.

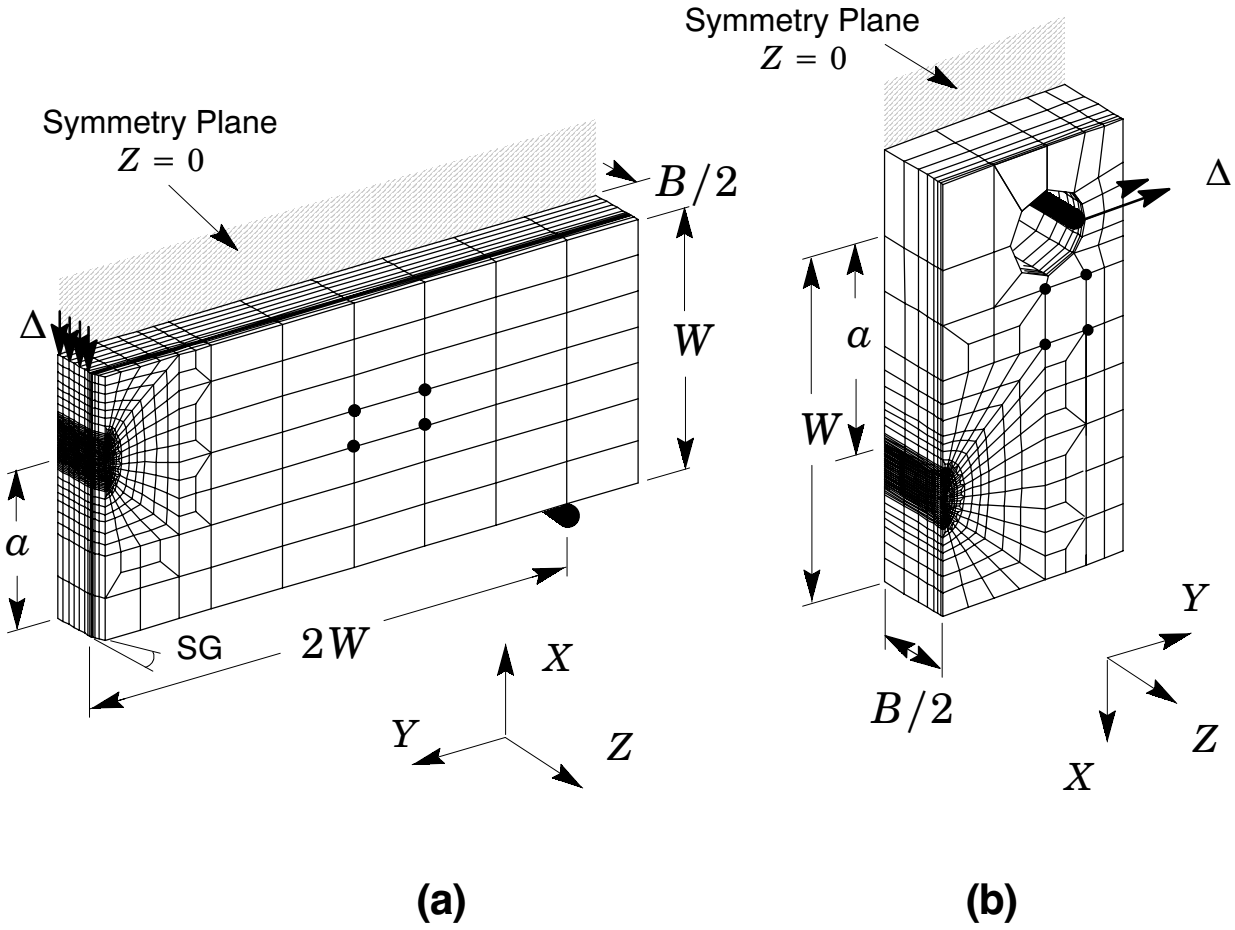

Figure 2 *Finite element models employed in the analyses.*

4. NUMERICAL RESULTS AND COMPARISON WITH EXPERIMENTS

4.1. Constraint Effects on R-Curve

This section describes the results of detailed 3-D analyses to predict R-curves for the deep and shallow notch SE(B) specimens tested by Joyce and Link [15]. Figure 3(a) shows the predicted J-resistance curves for the SE(B) specimens computed using $f_0 = 0.002$, $D = 250\,\mu$m with the acceleration parameters assigned the values $\epsilon_N = 0.75$, $s_N = 0.05$ and $f_N = 0.50$ (R&D [11]). For each a/W ratio, tests were performed on three nominally identical specimens; the experimental data are indicated with symbols. The solid line in the plot represents a *mean* resistance

curve obtained by a weighted average taken over the half-thickness. The dashed line represents the computed resistance curve for crack extension defined at the centerplane ($Z = 0$).

The calibration process to set values for these parameters used experimental results for only the deep notch R-curve. The prediction effort then focused on the shallow notch specimen. The centerplane and average resistance curves generated in the 3-D analyses agree quite well with the experimental R-curves for 4-5 mm of crack extension. The centerplane and thickness average R-curves bracket the three experimental data sets for each a/W ratio. Note that the experimental crack extensions shown in this figure derive from the unloading compliance estimates and thus represent some average crack growth over the front. Also recall that the layer of 60 computational cells defined ahead of each point along the initial crack front allows maximum growth of 7.5 mm ($60 \times D/2$). However, at crack extensions beyond the ≈ 5 mm range, it seems reasonable to expect some influence on the R-curve from the non-voided, background material ahead of the 7.5 mm limit as the crack front at the side-groove in the shallow notch specimens exhausts the 60 cells at ≈ 4 mm of growth on the centerplane. Detailed studies of the porosity distribution on the crack plane suggest that the decreasing slopes observed in R-curves follow from the continually expanding size of the process zone for void growth on the crack plane [11]. In the analyses, cells at increasingly larger distances from the crack front experience void growth. Consequently, as the crack front extends to their location, little additional deformation is required to attain $f = f_E$.

4.2. R-Curve Response and Crack Front Tunneling for C(T) Specimens

Panontin and Nishioka [16] performed unloading compliance tests at room temperature on 1T-C(T) specimens of an A516-70 steel. The specimens have $a/W = 0.6$ but do not have side-grooves. The measured resistance and load-displacement curves for tests performed were obtained using two different orientations of the crack plane relative to the rolling direction of the steel plate. In the TL orientation, the crack grows in the rolling direction of the plate, i.e., crack growth is aligned with the elongated grain structure. In the LT orientation, crack growth occurs transverse to the rolling direction. The computed R-curves using the cell model outlined previouly agree well with experimental data (see detais in R&D [11]).

Figure 3(b) compares the measured crack front profile for the LT specimen with the front profile predicted by the 3-D analysis. The unloading compliance test was interrupted at a J of 510 kJ/m^2; the specimen was fatigue cycled to mark the end of ductile tearing, and finally loaded to fracture. The predicted crack front indicated on the figure is obtained by adding the measured fatigue pre-crack to the numerical results at each point along the crack front (predicted growth values taken at J of 510 kJ/m^2). Generally good agreement exists between the computed and the measured crack-front shape; the analysis captures the features of the extending crack front, especially in the mid-thickness region. At the quarter-thickness location, the measured front has less growth and less curvature than the predicted curve, perhaps an effect of the curved fatigue pre-crack.

5. CONCLUDING REMARKS

This study describes a 3-D computational framework to model stable extension of a macroscopic crack under mode I conditions in ductile metals. Material separation occurs through a local fracture mechanism based on the growth and coalescence of microvoids dispersed in the material. The Gurson-Tvergaard dilatant plasticity model for voided materials describes the eventual loss of material stress capacity under sustained loading. Fixed-size computational cell elements defined on a thin layer adjacent to the crack plane provide an explicit length scale for the continuum damage model. An element vanish procedure removes highly voided cells from further consideration in the analysis, thereby creating new traction-free surfaces which extend the macroscopic crack. The key micromechanics parameters are D, the thickness of the computational cell layer, and f_0, the initial cell porosity. These parameters are calibrated

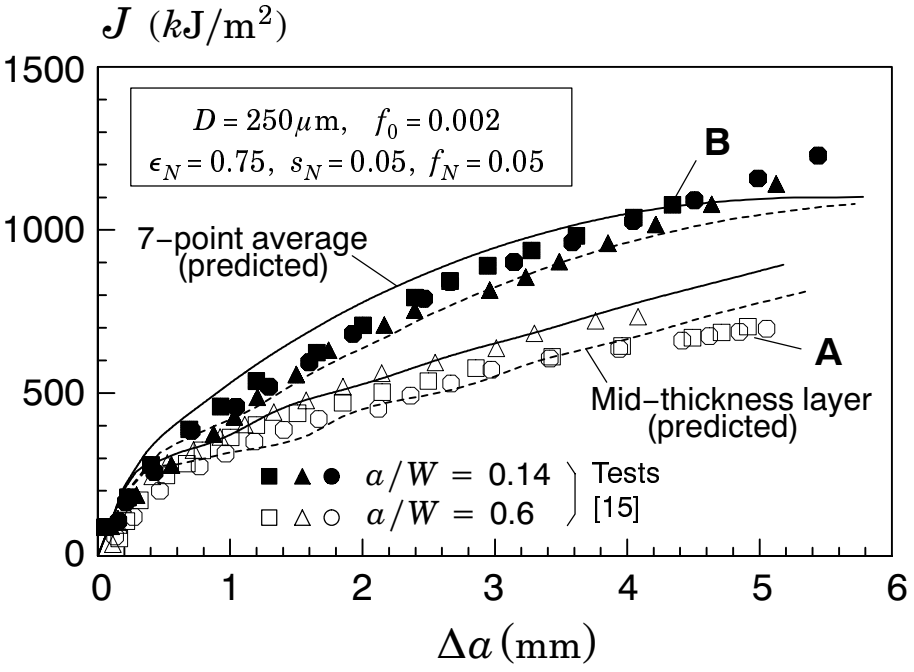

(a)

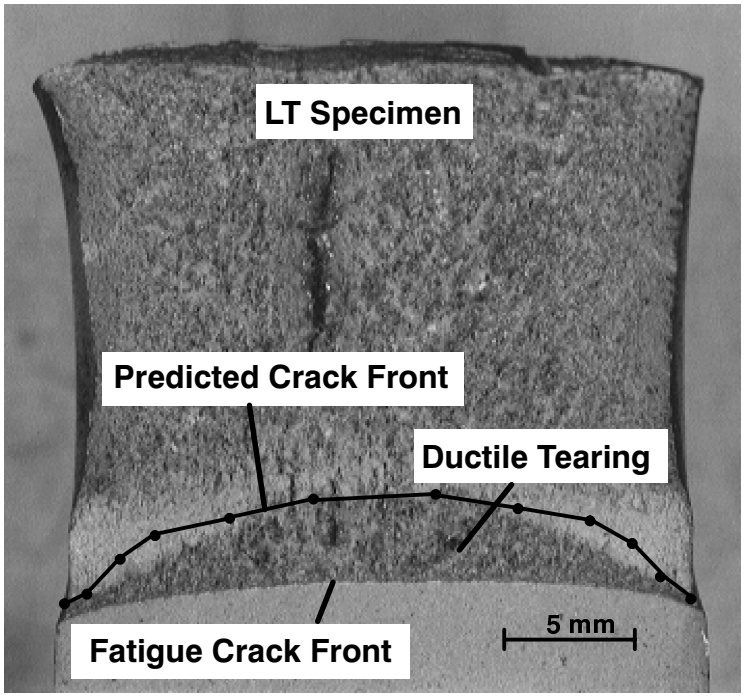

(b)

Figure 3 *(a) Predicted R-curve for the A533 steel; (b) Predicted crack front for the A516 steel.*

through analyses of ductile tearing to match R-curves obtained by testing simple through-crack specimens. Such calibration scheme provides *computational* parameters which are loosely coupled, at best, with metallurgical features of the material. The resulting computational framework, coupled with refined 3-D meshes, enables the detailed study of non-uniform growth along the crack front, including tunneling and reverse tunneling, and predictions of specimen size, geometry and loading mode effects on tearing resistance, here described by J-Δa curves.

Our exploratory 3-D analyses of deep and shallow crack SE(B) specimens and of a deep crack C(T) specimen demonstrate the capability to predict geometry effects on R-curves and measured crack front profiles. In particular, numerical results for the plane-sided C(T) specimen predict a tunneled crack front profile in very good agreement with the post-test, measured profile. Our computations also predict remarkably well the (strong) effects of constraint on measured R-curves for the side-grooved SE(B) specimens.

The computational demands for refined 3-D analyses of ductile growth remain formidable. However, the numerical procedures described here coupled with the newest generation of Unix workstations are making feasible these analyses on a more routine basis. Ongoing work with the 3-D computational cell framework focuses on modeling of ductile tearing in surface cracks in pipelines/cylinders to resolve R-curve transferability issues and on the effects of ductile tearing as the precursor to cleavage fracture in the ductile-to-brittle regime (see [NO TAG] for initial studies).

Acknowledgements

Funding to the first author (CR) was provided by Fundação de Amparo à Pesquisa do Estado de São Paulo (FAPESP) under grant 95/9898-0. The work of RD was supported by grants from the U.S. Nuclear Regulatory Commission, the Naval Surface Warfare Center and the NASA-Ames Research Center. Access to Cray C-90 computers was provided by the National Aerodynamic Simulator facility (NAS) at NASA-Ames and by a grant of HPC resources from the DoD HPC Centers at the Waterways Experiment Station and the Stennis Space Center. The authors acknowledge the many useful discussions and contributions of their colleagues Prof. C. Fong Shih (Brown University) and Profs. Rick Link and Jim Joyce (U.S. Naval Academy).

References

1. Hutchinson, J.W., "Fundamentals of the Phenomenological Theory of Nonlinear Fracture Mechanics," *Journal of Applied Mechanics*, Vol. 50, pp. 1042–1051, 1983.
2. Varias, A. G. and Shih, C. F., "Quase–Static Crack Advance Under a Range of Constraints – Steady State Fields Based on a Characteristic Length", *Journal of the Mechanics and Physiscs of Solids*, Vol. 41, pp. 835–861, 1993.
3. Dodds, R. H., Tang, M. and Anderson, T. L., "Effects of Prior Tearing on Cleavage Fracture Toughness in the Transition Region" in *Constraint Effects in Fracture, Theory and Application*, ASTM STP 1244, M. Kirk and A. Bakker, Eds., American Society for Testing and Materials, Philadelphia, Pennsylvania, 1993.
4. *Constraint Effects in Fracture, ASTM STP 1171*, Hackett, et al. Eds., American Society for Testing and Materials, Philadelphia, 1993.
5. Xia, L. and Shih, C. F., "Ductile Crack Growth - I. A Numerical Study Using Computational Cells with Microstructurally-Based Length Scales," *Journal of the Mechanics and Physics of Solids*, Vol. 43, pp. 233-259, 1995.
6. Xia, L. and Shih, C. F., "Ductile Crack Growth - II. Void Nucleation and Geometry Effects on Macroscopic Fracture Behavior," *Journal of the Mechanics and Physics of Solids*, Vol. 43, pp. 1953–1981, 1995.
7. Xia, L. and Shih, C. F., "Ductile Crack Growth - III. Statistical Aspects of Cleavage Fracture After Tearing," *Journal of the Mechanics and Physics of Solids,* Vol. 44, pp. 603–639, 1996.
8. Gurson, A. L., "Continuum Theory of Ductile Rupture by Void Nucleation and Growth: Part I - Yield Criteria and Flow Rules for Porous Ductile Media," *Journal of Engineering Materials and Technology*, Vol. 99, pp. 2-15.
9. Tvergaard, V., "Material Failure by Void Growth to Coalescence," *Advances in Applied Mechanics*, Vol. 27, pp. 83-151, 1990.
10. Garrison, W. M, Jr. and Moody, N. R., "Ductile Fracture," *Journal of the Physics and Chemistry of Solids*, Vol. 48, pp. 1035-1074, 1987.

11. Ruggieri, C. and Dodds, R. H., "Numerical Modeling of Ductile Crack Growth in 3-D Using Computational Cell Elements," *International Journal of Fracture*, Vol. 82, pp. 67-95, 1996.

12. Chu, C. C. and Needleman, A., "Voids Nucleation Effects in Biaxially Stretched Sheets," *Journal of Engineering Materials and Technology*, Vol. 102, pp. 249-256, 1980.

13. Koppenhoefer, K., Gullerud, A., Ruggieri, C., Dodds, R. and Healy, B., "WARP3D: Dynamic Nonlinear Analysis of Solids Using a Preconditioned Conjugate Gradient Software Architecture", *Structural Research Series (SRS) 596*, UILU-ENG-94-2017, University of Illinois at Urbana-Champaign, 1994.

14. Moran, B., and Shih, C.F., "A General Treatment of Crack Tip Contour Integrals," *International Journal of Fracture,* Vol. 35, pp. 295-310, 1987.

15. Joyce, J. A., and Link, R. E., "Effects of Constraint on Upper-Shelf Fracture Toughness," *Fracture Mechanics: 26th Volume, ASTM STP 1256*, Reuter, W. G., Underwood, J. H., and Newman, J. C. Eds., American Society for Testing and Materials, Philadelphia, pp. 142-177, 1995.

16. Panontin, T.L. and Nishioka, O., private communication.